

Influence of strain and pressure to the effective refractive index of the fundamental mode of hollow-core photonic bandgap fibers

M. Pang, H. F. Xuan, J. Ju, and W. Jin*

Department of Electrical Engineering, Hong Kong Polytechnic University, Hong Kong, China
*ewjin@polyu.edu.hk

Abstract: We investigate the phase sensitivity of the fundamental mode of hollow-core photonic bandgap fibers to strain and acoustic pressure. A theoretical model is constructed to analyze the effect of axial strain and acoustic pressure on the effective refractive index of the fundamental mode. Simulation shows that, for the commercial HC-1550-02 fiber, the contribution to the overall phase sensitivities to axial strain and acoustic pressure are respectively $\sim 2\%$ and $\sim 17\%$. The calculated normalized phase-sensitivities of the HC-1550-02 fiber to strain and acoustic pressure are respectively $1 \text{ } \epsilon^{-1}$ and $-331.6 \text{ dB re } \mu\text{Pa}^{-1}$ without considering mode-index variation, and $0.9797 \text{ } \epsilon^{-1}$ and $-333.1 \text{ dB re } \mu\text{Pa}^{-1}$ when mode-index variation is included in the calculation. The latter matches better with the experimentally measured results.

©2010 Optical Society of America

OCIS codes: (060.2370) Fiber optics sensors; (120.5050) Phase measurement; (060.5295) Photonic crystal fibers.

References and links

1. C. K. Kirkendall, and A. Dandridge, "Overview of high performance fiber-optic sensing," *J. Phys. D* **37**(18), R197–R216 (2004).
2. V. Dangui, H. K. Kim, M. J. F. Digonnet, and G. S. Kino, "Phase sensitivity to temperature of the fundamental mode in air-guiding photonic-bandgap fibers," *Opt. Express* **13**(18), 6669–6684 (2005).
3. H. K. Kim, M. J. F. Digonnet, and G. S. Kino, "Air-core photonic-bandgap fiber-optic Gyroscope," *J. Lightwave Technol.* **24**(8), 3169–3174 (2006).
4. M. Pang, and W. Jin, "Detection of acoustic pressure with hollow-core photonic bandgap fiber," *Opt. Express* **17**(13), 11088–11097 (2009).
5. L. J. Gibson, and M. F. Ashby, *Cellular solids: structure and properties, second edition*, (Cambridge University Press, New York 1997).
6. R. M. Christensen, "Mechanics of cellular and other low-density materials," *Int. J. Solids Struct.* **37**(1-2), 93–104 (2000).
7. S. P. Timoshenko, and J. Goodier, *Theory of Elasticity* (McGraw-Hill, New York, 1970).
8. A. Cucnotta, S. Selleri, L. Vincetti, and M. Zoboli, "Holey fiber analysis through the finite element method," *IEEE Photon. Technol. Lett.* **14**(11), 1530–1532 (2002).
9. J. Ju, W. Jin, and M. S. Demokan, "Properties of a Highly Birefringent Photonic Crystal Fiber," *IEEE Photon. Technol. Lett.* **15**(10), 1375–1377 (2003).
10. J. D. Shephard, P. J. Roberts, J. D. C. Jones, J. C. Knight, and D. P. Hand, "Measuring Beam Quality of Hollow Core Photonic Crystal Fibers," *J. Lightwave Technol.* **24**(10), 3761–3769 (2006).
11. Y. L. Su, Y. Q. Wang, Z. G. Zhao, and Y. L. Kang, *Mechanics of Materials* (Tianjin Univ. Press, China 2001).
12. K. Saitoh, N. Mortensen, and M. Koshiba, "Air-core photonic band-gap fibers: the impact of surface modes," *Opt. Express* **12**(3), 394–400 (2004).
13. C. D. Butter, and G. B. Hocker, "Fiber optics strain gauge," *Appl. Opt.* **17**(18), 2867–2869 (1978).
14. Crystal Fiber website, <http://www.nktpotonics.com/>

1. Introduction

Optical fiber sensor is a subject of continuing interest, because of its high sensitivity and reliability, EMI immunity, cost-effectiveness, electrically passive operation, and multiplexing and distributed sensing capability [1]. Hollow-core photonic bandgap fiber (HC-PBF) interferometric sensors have attracted considerable interest recently, because of their unique

responses to strain, temperature, pressure, and etc. HC-PBF-based interferometric fiber gyroscopes and hydrophones have demonstrated improved performance as compared with their conventional fiber counterparts [2–4].

Assume that the sensing HC-PBF has a length L , the effective index of fundamental mode is n_{eff} , and the operating light wavelength in vacuum is λ , the phase (φ) accumulated by the fundamental mode travelling through this section of HC-PBF is given by Eq. (1).

$$\varphi = \frac{2\pi}{\lambda} n_{eff} L \quad (1)$$

The (normalized) phase sensitivity of the fundamental mode to a measurand “ X ” may be generally expressed as

$$S = \frac{1}{\varphi} \frac{d\varphi}{dX} = \frac{1}{L} \frac{dL}{dX} + \frac{1}{n_{eff}} \frac{dn_{eff}}{dX} = S_L + S_n, \quad (2)$$

where “ X ” can be temperature, (acoustic) pressure, fiber elongation (compression), and etc. In the right-hand side of Eq. (2), the first term (S_L) is a length-term that represents the measurand-induced physical change of the fiber length, and the second term (S_n) is an index-term representing the measurand-induced change of the effective refractive index of the fundamental mode. The index-term is due to the sum of two effects: the deformation of in-profile configuration of the HC-PBF, which modifies the size of hollow-core, the sizes and the shapes of the microstructure cladding cells; and the change of the refractive index of the fiber material through elasto-optic effect. Since the axial strain (ε) is related to fiber elongation (compression) ($dX = dL$) by $\varepsilon = dL/L$, the normalized phase sensitivity of the fundamental mode to axial strain, which is preferred in some applications, may be expressed as Eq. (3).

$$S = \frac{1}{\varphi} \frac{d\varphi}{\varepsilon} = \frac{L}{\varphi} \frac{d\varphi}{dL} = 1 + \frac{L}{n_{eff}} \frac{dn_{eff}}{dL} = 1 + \frac{1}{n_{eff}} \frac{dn_{eff}}{\varepsilon} = S_L + S_n \quad (3)$$

We have studied the response of the fundamental mode phase of HC-PBFs to acoustic pressure and demonstrated that, for optimized the fiber parameters, the phase sensitivity in terms of normalized responsivity to acoustic pressure ($NR = 20 \log |S|$) can be increased by as much as 35dB ($S = \sim 60$ times) over the conventional single mode fiber [4]. This significant improvement of the sensitivity would simplify the design of interferometric fiber optic hydrophone arrays and reduce the system cost [1]. In the theoretical analysis reported in [4], we neglected the change in the index-term to the sensors’ phase sensitivity, because most of light power of the fundamental mode in a HC-PBF travels in the air and length-term should be dominant. However, strain and stress applied to the HC-PBF do change the in-profile configuration of the fiber’s microstructure cladding and the index of the fiber material, which affect the fundamental-mode effective index.

In this paper, we report a theoretical model for evaluating the effect of strain and stress on the effective refractive index of the fundamental-mode of HC-PBF. The microstructure cladding of the HC-PBF is firstly considered as a layer of anisotropic material and the fiber’s strain and stress distributions in different layers are calculated by using the theory of elasticity [5–7]. Based on the strain and stress distributions, the deformation and displacement of each cell and the detailed change of in-profile configuration of the fiber are then derived. By using the elasto-optic effect, the material index distribution of the microstructure cladding is also obtained. The effective index of the fundamental-mode is then determined by the finite element analysis solver (COSMOL) [8,9].

The theoretical model is used to evaluate the effect of axial strain and (acoustic) pressure on the effective index of the fundamental-mode. The modeling results are found in good agreement with the experimental results obtained from the commercial HC-1550-2 PBF.

2. Theoretical Modeling

2.1 Elasticity model of HC-PBF

The mechanical model for computing the strain and stress of HC-PBF under different boundary conditions was described in Ref [4]. The HC-PBF may be modeled as a structure (Fig. 1) with four circular regions: region 0 is the air core with radius of a ; region 1 is the microstructure cladding (honeycomb cladding) with thickness of $b-a$; region 2 is the silica outer-cladding with thickness of $c-b$; and finally they are coated with a jacket region to the radius of d .

Each layer is characterized by a certain elastic modulus E and Poisson's ratio ν . The materials of silica outer-cladding and jacket regions are homogeneous, and their Young's modulus and Poisson's ratios are E_2, E_3 , and ν_2, ν_3 respectively. The microstructure cladding of the HC-PBF is an exception in that it is not a homogeneous material but it behaves mechanically like a honeycomb [5,6]. The Young's modulus and Poisson's ratio of a honeycomb are functions of air-filling ratio η . For a hexagonal pattern of air holes in silica, they are given by [5]:

$$\begin{cases} E_r = E_\theta = \frac{3}{2}(1-\eta)^3 E_0 = E_1^* \\ E_z = (1-\eta)E_0 = E_1 \end{cases} \quad \begin{cases} \nu_{r-\theta} = \nu_{\theta-r} = 1 \\ \nu_{z-\theta} = \nu_{z-r} = \nu_1, \\ \nu_{r-z} = \nu_{\theta-z} \approx 0 \end{cases} \quad (4)$$

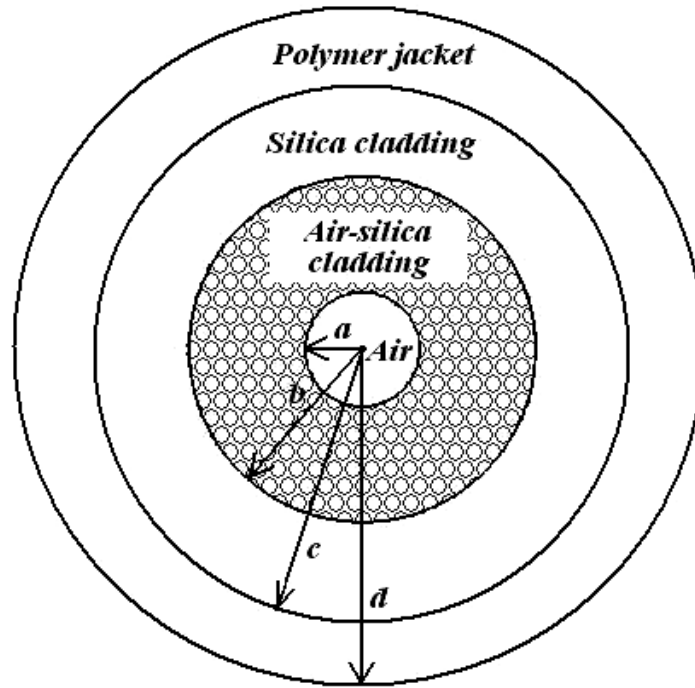


Fig. 1. Configuration of a HC-PBF with an air-core, a honeycomb air-silica inner-cladding, a solid-silica outer-cladding and a polymer jacket.

where E_0 and ν_1 are the Young's modulus and Poisson's ratio of the silica material; E_r, E_θ, E_z are the effective Young's modulus of the silica-air honeycomb in the three directions, and $\nu_{r-\theta}, \nu_{\theta-r}, \nu_{z-\theta}, \nu_{\theta-z}, \nu_{r-z},$ and ν_{z-r} are the six Poisson's ratio items of the honeycomb.

The stress expressions of the three regions may be expressed as [7]:

$$\begin{cases} \sigma_r^i = \frac{A_i}{r^2} + 2C_i \\ \sigma_\theta^i = -\frac{A_i}{r^2} + 2C_i, \\ \sigma_z^i = D_i \end{cases} \quad (5)$$

where A_i , C_i , and D_i ($i = 1, 2$ and 3) are constants. Using Hooke's law, we obtain the strain tensors of different layers shown as:

$$\begin{cases} \varepsilon_r^1 = \frac{2A_1}{E_1 r^2} - \nu_1 \frac{D_1}{E_1} \\ \varepsilon_\theta^1 = -\frac{2A_1}{E_1 r^2} - \nu_1 \frac{D_1}{E_1} \\ \varepsilon_z^1 = \frac{D_1}{E_1} \end{cases} \quad \begin{cases} \varepsilon_r^i = \frac{1}{E_i} [(1 + \nu_i) \frac{A_i}{r^2} + 2(1 - \nu_i) C_i - \nu_i D_i] \\ \varepsilon_\theta^i = \frac{1}{E_i} [-(1 + \nu_i) \frac{A_i}{r^2} + 2(1 - \nu_i) C_i - \nu_i D_i] \\ \varepsilon_z^i = \frac{1}{E_i} (D_i - 4\nu_i C_i) \end{cases} \quad (i = 2, 3) \quad (6)$$

There are nine constants to be determined: A_i , C_i , D_i ($i = 1, 2$ and 3). To determine these constants when subject to different measurands, different boundary conditions need to be used. When the HC-PBF is subject to acoustic pressure, the boundary conditions and the stresses and strains of each layers of the HC-PBF have been given in Ref [4]. When the fiber is subject to axial strain ε , the boundary conditions may be expressed as:

$$\begin{aligned} \sigma_r^1 \Big|_{r=b} &= \sigma_r^2 \Big|_{r=b} & (a) \\ \sigma_r^2 \Big|_{r=c} &= \sigma_r^3 \Big|_{r=c} & (b) \\ u_r^1 \Big|_{r=b} &= u_r^2 \Big|_{r=b} & (c) \\ u_r^2 \Big|_{r=c} &= u_r^3 \Big|_{r=c} & (d) \\ \sigma_r^1 \Big|_{r=a} &= 0 & (e) \\ \sigma_r^3 \Big|_{r=d} &= 0 & (f) \\ \varepsilon_z^1 = \varepsilon_z^2 = \varepsilon_z^3 &= \varepsilon & (g), \end{aligned} \quad (7)$$

where u_r^i is the radial displacement in region i , which is related to strain by Eq. (8). Equation (7a) and (7b) describe radial stress continuity across the boundaries of regions; Eq. (7c) and Eq. (7d) describe the radial displacement continuity across the boundaries of the regions; Eq. (7e) and (7f) means the core and the outer regions of fiber are air; Eq. (7g) is for the plane approximation [7], which ignores end effects.

$$u_r^i = \int \varepsilon_r^i dr \quad (8)$$

By using Eqs. (5), (6), (7) and (8), the constants A_i , C_i , and D_i can be determined. Hence the stress, strain and displacement distributions of each layer of the HC-PBF can be obtained. We here are interested in the stress, strain and displacement of the microstructure region, i.e., σ_r^1 , σ_θ^1 , σ_z^1 , ε_r^1 , ε_θ^1 , ε_z^1 , and u_r^1 , from which the field and effective refractive index variations of the fundamental mode may be evaluated by following the procedure as outlined in the next section.

2.2 Change of microstructure cladding profile

Now we are in the position to calculate the change in the transverse profile of the microstructure cladding by using the stress, strain and displacement distributions obtained in

Section 2.1. The profile change modifies the waveguide structure and hence the effective index of fundamental mode. Consider an arbitrary cell centered at (r, θ) , as shown in Fig. 2(1), the in-profile stresses acting on this cell may be written as σ'_r and σ'_θ , as shown in Fig. 2(2) and Fig. 2(3). σ'_r may be decomposed into three components: the x - and y -directional stresses $\sigma'^l_{r,x}$ and $\sigma'^l_{r,y}$, and the shear $\tau'^l_{r,xy}$, which are respectively given by [11]:

$$\begin{cases} \sigma'^l_{r,x} = \sigma'_r \cos^2(\theta) \\ \sigma'^l_{r,y} = \sigma'_r \sin^2(\theta) \\ \tau'^l_{r,xy} = \sigma'_r \sin(\theta)\cos(\theta) \end{cases} \quad (9)$$

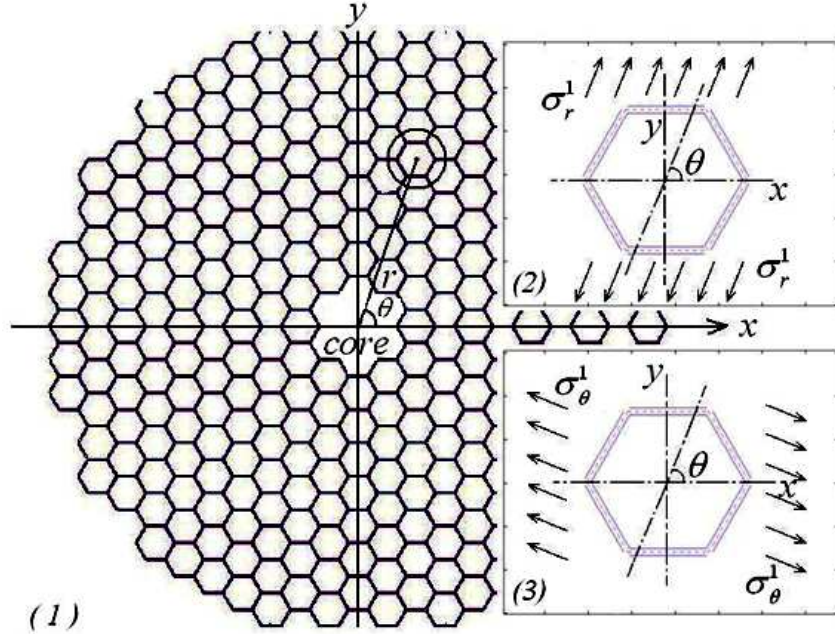


Fig. 2. (1) Profile configuration of the HC-PBF's microstructure cladding; (2) In-profile stress σ'_r on a cell of the microstructure cladding; (3) In-profile stress σ'_θ on a cell of the microstructure cladding.

The deformation of the cell under load σ'_r is the sum of the deformations under loads $\sigma'^l_{r,x}$, $\sigma'^l_{r,y}$ and $\tau'^l_{r,xy}$ as shown in Fig. 3, and the deformations of the cell walls (1~6) due to each of the load components are calculated respectively as follows [5]:

2.2.1 Deformation due to $\sigma'^l_{r,x}$

As Fig. 3(1) shows, when the cell under the load $\sigma'^l_{r,x}$ deforms in a linear-elastic way, the cell walls 1 and 4 keep straight and the walls 2, 3, 5 and 6 bend by following a similar pattern. In the new set of coordinates $\{x', y'\}$, the moment of the wall 2 may be written as:

$$M_x = -\frac{\sqrt{3}}{2}Wx', \quad (10)$$

where $W = (\sqrt{3}/2)el\sigma'^l_{r,x}$, l is the length of the cell wall and e is unit depth in z -direction. The subscript "x" means the moment is caused by $\sigma'^l_{r,x}$. Then the deformation of cell wall 2 along the y' direction as the function of x' can then be obtained by double integration of Eq. (10) with respect to x' and with proper boundary conditions and expressed as

$$V_{y,x} = -\frac{\sqrt{3}W}{2E_0I} \left[\frac{(x'+l/2)^3}{6} - \frac{l(x'+l/2)^2}{4} + \frac{l^3}{24} \right], \quad (11)$$

where $I = et^3/12$, t is the thickness of the wall. The subscripts “y”, “x” means the displacement is along y'-direction and is caused by $\sigma'_{r,x}$.

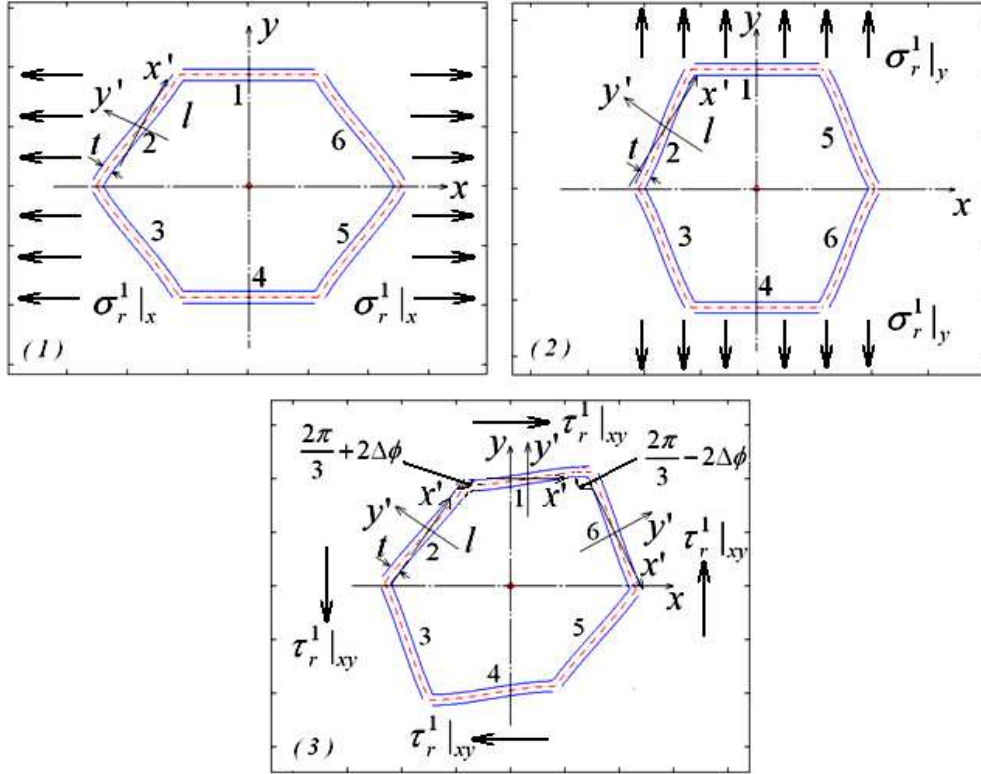


Fig. 3. The deformation of the cell under loads $\sigma'_{r,x}$, $\sigma'_{r,y}$ and $\tau'_{r,xy}$ respectively.

2.2.2 Deformation due to $\sigma'_{r,y}$

In Fig. 3(2), when the cell under the load $\sigma'_{r,y}$ deforms in a linear-elastic way, the cell walls 1 and 4 keep straight and walls 2, 3, 5 and 6 bend. In the new set of coordinates $\{x', y'\}$, the moment of the wall 2 can be written as:

$$M_y = \frac{1}{2} P x', \quad (12)$$

where $P = (3/2)el\sigma'_{r,y}$. The subscript “y” means the moment is caused by $\sigma'_{r,y}$. The deformation of cell wall 2 as the function of x' can be obtained from Eq. (12) and expressed as Eq. (13).

$$V_{y',y} = \frac{P}{2E_0I} \left[\frac{(x'+l/2)^3}{6} - \frac{l(x'+l/2)^2}{4} + \frac{l^3}{24} \right] \quad (13)$$

The subscripts “y”, “y” means the deformation is along y'-direction and is caused by $\sigma'_{r,y}$.

2.2.3 Deformation due to $\tau'_{r,xy}$

The deformation of the cell under shear $\tau'_{r,xy}$ is shown in Fig. 3(3). According to knowledge of cellular solids [5], when the honeycomb cell is sheared, all of cell walls bend, and walls 2, 3, 5, 6 will rotate compared with their original positions. The angle of rotation ($\Delta\phi$) can be written as:

$$\Delta\phi = \frac{Fl^2}{24E_0I}, \quad (14)$$

where $F = \sqrt{3}l\epsilon\tau'_{r,xy}$. Because of symmetry, the cell walls 4 and 1, 5 and 2, 3 and 6 have similar bending patterns respectively. In their own new set of coordinates, the moments of walls 1, 2 and 6 can be written as:

$$\begin{cases} M_{\tau_1} = Fx' \\ M_{\tau_2} = -\frac{F}{2}x' \\ M_{\tau_6} = -\frac{F}{2}x' \end{cases} \quad (15)$$

The deformations of walls 1, 2 and 6 in the y' -direction as the function of x' can be calculated from Eq. (15) and expressed as Eq. (16). The subscripts " y' , τ_i " means the deformation is along y' -direction and is caused by the shear $\tau'_{r,xy}$ acting on the " i^{th} " wall. It should be emphasized that the coordinates $\{x', y'\}$ for different walls are different and the deformation for a particular wall is expressed in the coordinates of that wall.

$$\begin{aligned} V_{y';\tau_1} &= \frac{F}{E_0I} \left[\frac{(x'+l/2)^3}{6} - \frac{l(x'+l/2)^2}{4} + \frac{l^3}{24} \right] \\ V_{y';\tau_2} &= \frac{F}{E_0I} \left[\frac{(x'+l/2)^3}{6} - \frac{l(x'+l/2)^2}{4} + \frac{l^3}{24} \right] \\ V_{y';\tau_6} &= \frac{F}{E_0I} \left[\frac{(x'+l/2)^3}{6} - \frac{l(x'+l/2)^2}{4} + \frac{l^3}{24} \right] \end{aligned} \quad (16)$$

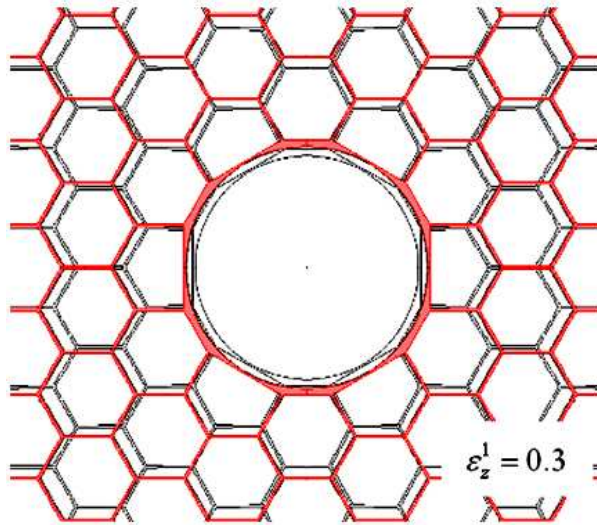


Fig. 4. Deformed profile (black) of HC-PBF, when the fiber is under the axial straining of $\epsilon_z^1 = 0.3$. For comparison, the original profile is shown in red.

Using Eqs. (11), (13), (14) and (16), we can obtain the deformation of the cell due to load σ'_r . The deformation of the cells due to σ'_θ can be obtained by following a similar process. The total deformation is the sum of deformations due to σ'_r and σ'_θ . By using Eqs. (6) and (8), we can then plot the new transverse profile of the deformed fiber. For example, Fig. 4 shows the transverse profile of the HC-PBF when it is subjected to axial straining of $\varepsilon'_z = 0.3$. In this Figure, the black pattern shows the deformed profile, while the red one shows the original profile of the HC-PBF. In the calculation, the following fiber parameters are used: *Pitch* = $3.8\mu\text{m}$, air-filling ratio $\eta = 94\%$, $a = 5.45\mu\text{m}$, $b = 35\mu\text{m}$ and $c = 60\mu\text{m}$. All the cladding cells, except the ones in the innermost ring, are regarded as ideal honeycomb hexagons as shown in Fig. 2. For the 12 cells near the core surround, 6 of them keep the original hexagonal shape while the other 6 are modified with the two sides of the hexagons are replaced by a straight line that connects the two corners of the original hexagons [12]. The core surround is approximated from the actual core shape (shown in Fig. 11) and is formed by silica sandwiched in-between the sides of the innermost cells and a circle centered at the fiber axis and with a radius of $r = a + u_r|_{r=a}$. The strain and displacement of the core surround was calculated directly from Eqs. (5), (6), (7) and (8); while Eqs. (11), (13), (14) and (16) are also needed to obtain the deformations of the cell walls.

In addition to the change of transverse geometry profile, the refractive index distribution of the material is also modified through strain-optic effect. The strain distribution within the wall cross-section is complex due to the compression (elongation) and bending of walls. For simplicity, we approximately regard the strain distribution is uniform along the direction normal to the wall (i.e., y' -axis) and equal to the strain along the center-line of the wall (i.e., along x' -axis). The walls that form the core-surround are treated in the same way as the walls of a uniform hexagon in the air-silica cladding. The strain-optic effect appears as a change in the optical indicatrix of the silica material [13]:

$$\Delta\left(\frac{1}{n^2}\right)_i = \sum_{j=1}^6 p_{ij} \begin{bmatrix} \frac{\sigma'_r}{E_1} - \nu_0 \frac{\sigma'_\theta}{E_1} - \nu_0 \varepsilon'_z \\ \frac{\sigma'_\theta}{E_1} - \nu_0 \frac{\sigma'_r}{E_1} - \nu_0 \varepsilon'_z \\ \varepsilon'_z \\ 0 \\ 0 \\ 0 \end{bmatrix}, \quad (17)$$

where p_{ij} is the strain-optic tensor, the subscripts are in the standard contracted notation, and n_0 is the original reflection index of the material. Silica material is a homogeneous isotropic medium and has only two numerical values p_{11} and p_{12} , thus the changes in the optical indices in the r , θ and z directions can be written as Eq. (18).

$$\begin{aligned} \Delta n_r &= -\frac{1}{2}n_0^3[(1-\nu_0)p_{12}\varepsilon'_z - \nu_0 p_{11}\varepsilon'_z + \frac{\sigma'_r - \nu_0\sigma'_\theta}{E_1} p_{11} + \frac{\sigma'_\theta - \nu_0\sigma'_r}{E_1} p_{12}] \\ \Delta n_\theta &= -\frac{1}{2}n_0^3[(1-\nu_0)p_{12}\varepsilon'_z - \nu_0 p_{11}\varepsilon'_z + \frac{\sigma'_\theta - \nu_0\sigma'_r}{E_1} p_{11} + \frac{\sigma'_r - \nu_0\sigma'_\theta}{E_1} p_{12}] \\ \Delta n_z &= -\frac{1}{2}n_0^3[\varepsilon'_z(p_{11} - 2\nu_0 p_{12}) + 2\frac{\sigma'_r - \sigma'_\theta}{E_1} p_{12}] \end{aligned} \quad (18)$$

Now, we have obtained the in-profile structure and material index distribution of the HC-PBF under difference conditions. The deformed profile and material index distribution are then imported into the finite element analysis solver (COSMOL) to compute the fundamental-mode profile and effective index of the fiber [8,9].

2.3 Predictions from the model

We applied the model described in sections 2.1 and 2.2 to calculate the effective index variation of the HC-1550-02 PBF when it is subjected to axial (longitudinal) strain and acoustic pressure. Table 1 shows the physical parameters of the HC-1550-02 fiber [14].

Table 1. Physical parameters of a commercial HC-PBF

| Fiber | Pitch | η | a | b | d | $E_0 = E_2$ |
|------------|-----------------------|-----------------|------------------------|----------------------|-----------------------|-------------|
| | 3.8 (μm) | 94% | 5.45 (μm) | 35 (μm) | 110 (μm) | 72 (GPa) |
| HC-1550-02 | E_3 | $\nu_1 = \nu_2$ | ν_3 | n_0 | p_{11} | p_{12} |
| | 0.5 (GPa) | 0.17 | 0.37 | 1.444 | 0.121 | 0.27 |

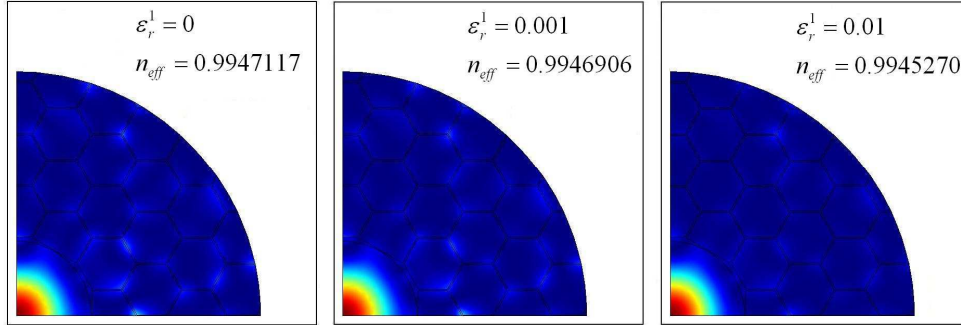


Fig. 5. The calculated intensity profiles and the effective refractive indices of the fundamental mode of HC-1550-02 fiber under different axial strains.

Figure 5 shows the calculated intensity profiles and refractive indices of the fundamental modes of HC-1550-02 under three different axial strain levels. The results shown in Fig. 5 are obtained from a model with four rings of air-silica cladding cells. The results from models with three and five rings of cladding cells were found no significant difference, because most of the light intensity is confined in the hollow-core and the cells near the core [10].

As discussed in Section 2.2, the change of the fundamental mode index are attributed to two factors: (1) the contribution of fiber geometry deformation (dn_{eff}/dX)_D; 2) the contribution of the fiber material index modification (dn_{eff}/dX)_N, as expressed in Eq. (19). Importing the model discussed in Section 2.1 and 2.2 into the finite element solver [8,9], the variation of the refractive index n_{eff} due to geometry deformation, material index, and their combination as the functions of the axial strain and acoustic pressure can be obtained. The results are shown respectively in Figs. 6(1) and 6(2).

$$\frac{dn_{eff}}{dX} = (dn_{eff}/dX)_D + (dn_{eff}/dX)_N \quad (19)$$

From Fig. 6(1), the slopes of the curves, i.e., $(dn_{eff}/\varepsilon)_D$, $(dn_{eff}/\varepsilon)_N$, and dn_{eff}/ε , are calculated to be $-0.0039 \varepsilon^{-1}$ and $-0.0162 \varepsilon^{-1}$, and $-0.0202 \varepsilon^{-1}$, respectively. Obviously the material index contribution is dominant and $(dn_{eff}/\varepsilon)_N$ is ~ 4 times larger than $(dn_{eff}/\varepsilon)_D$. This is because the fiber's in-profile deformation due to axial strain is considerably smaller than the axial deformation. Figure 7(1) shows the calculated ε_r^1 of the HC-PBF as the function of r , when the fiber is subjected to axial straining of $1\mu\varepsilon$. The material index change is mainly due to the relatively large strain along the axial direction. Substituting dn_{eff}/ε into Eq. (3), S_L , S_n , and S of HC-1550-02 may be estimated to be $1 \varepsilon^{-1}$, $-0.0203 \varepsilon^{-1}$, $0.9797 \varepsilon^{-1}$, respectively.

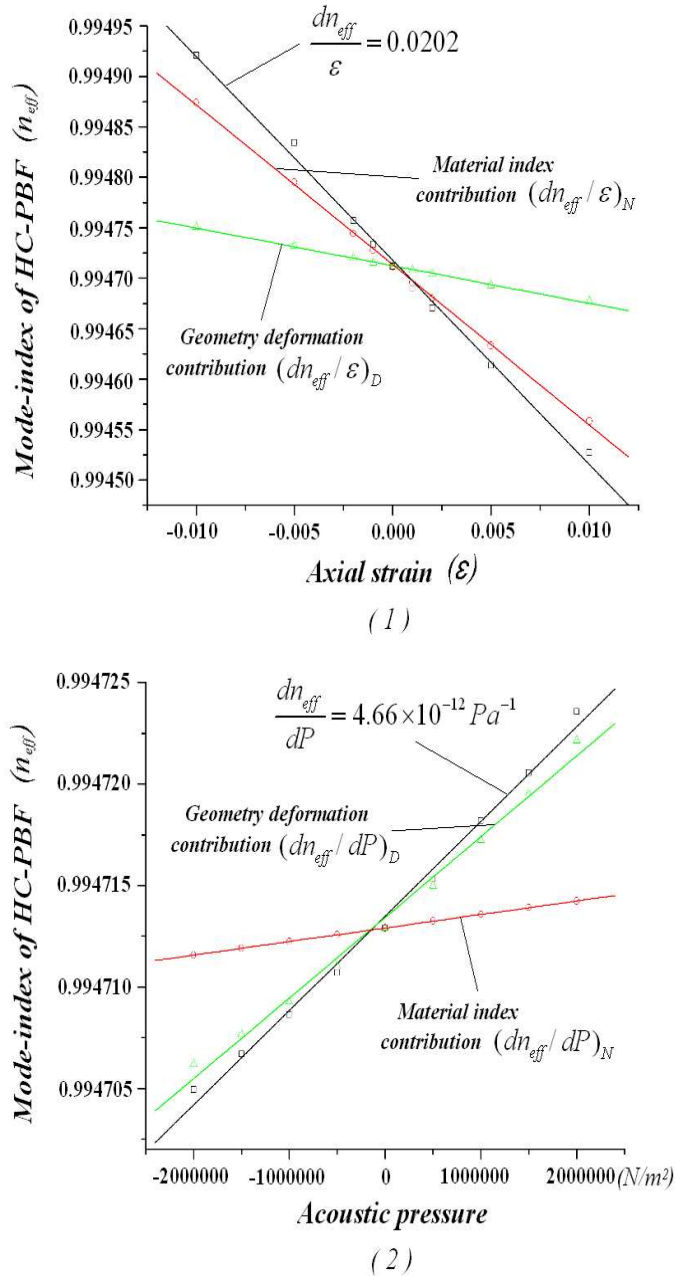


Fig. 6. HC-PBF's fundamental mode effective index (n_{eff}) as the functions of (1) axial straining and (2) acoustic pressure.

From Fig. 6(2), $(dn_{eff}/dP)_D$, $(dn_{eff}/dP)_N$ and dn_{eff}/dP , are estimated to be $3.97 \times 10^{-12} \text{Pa}^{-1}$, $6.66 \times 10^{-13} \text{Pa}^{-1}$ and $4.64 \times 10^{-12} \text{Pa}^{-1}$, respectively. The geometry deformation contribution $(dn_{eff}/dP)_D$ is dominant and is ~6 times larger than material index contribution $(dn_{eff}/dP)_N$. This is because that the acoustic pressure is applied to both axial and radial directions [4], and the simulation shows that in the fiber's air-silica cladding, the radial strain (ϵ_r^I) increases as r decreases and reaches its maximum when approaching to the core-cladding interface. Figure 7(2) shows ϵ_r^I as function of r acoustic pressure of $P = 10^3 \text{Pa}$. The large deformation

near the core region of air-silica cladding makes the fiber have a high $(dn_{eff}/dP)_D$. And as discussed in Section 2.2, this large deformation in air-silica cladding mainly comes from the bending of the honeycomb walls, but not the silica material strain. S , S_L and S_n can be calculated from Eq. (2) to be $-2.216 \times 10^{-11} \text{Pa}^{-1}$, $-2.68 \times 10^{-11} \text{Pa}^{-1}$ and $4.64 \times 10^{-12} \text{Pa}^{-1}$, respectively. The predicted NR (20log|S|) of HC-1550-02 PBF to acoustic pressure, is then $\sim 333.1 \text{dB re } 1 \mu\text{Pa}^{-1}$.

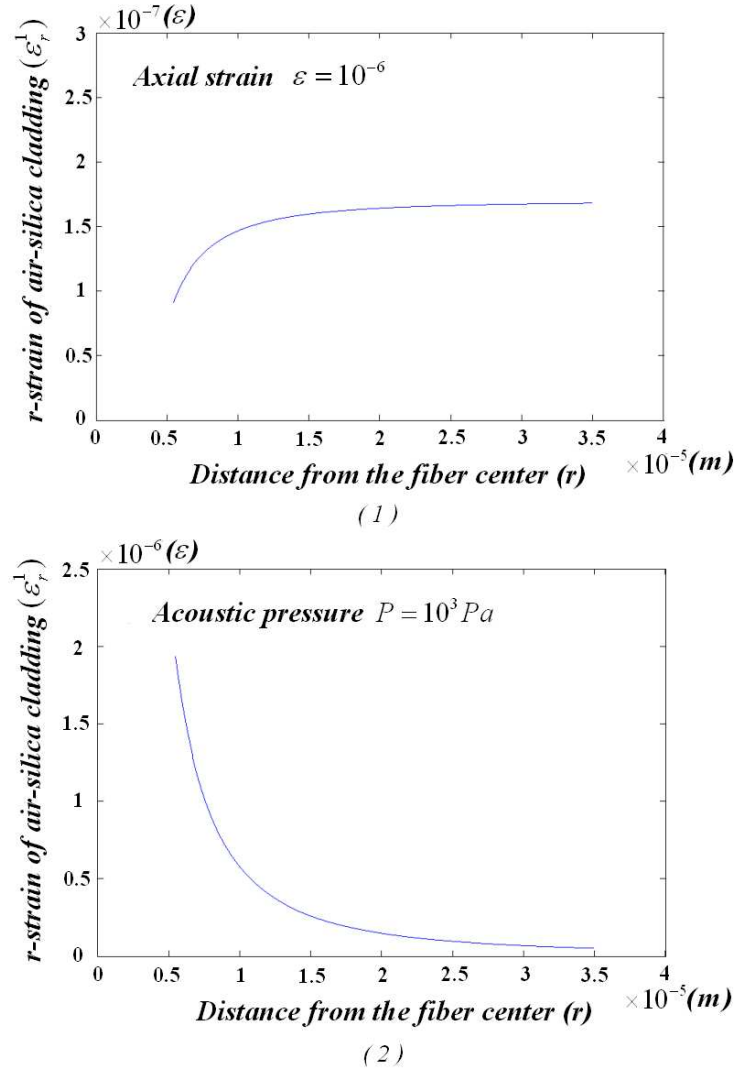


Fig. 7. Radial strain ϵ_r' in the HC-PBF's cladding for (1) an applied axial straining of $1 \mu\epsilon$ and (2) acoustic pressure of 10^3Pa .

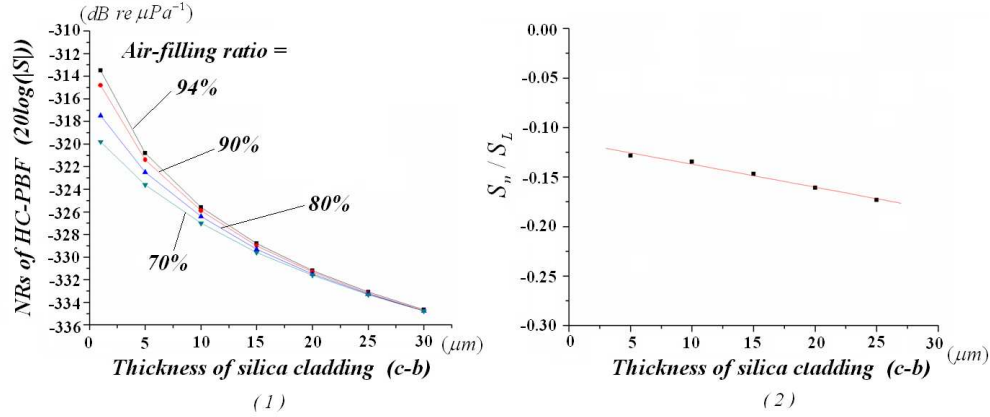


Fig. 8. (1) NR of HC-PBF as function of the thickness of the silica cladding ($c-b$) for different air filling ratios; (2) Calculated S_n/S_L of the HC-PBF as the function of ($c-b$), while other parameters are fixed at $a = 5.45\mu\text{m}$, $b = 35\mu\text{m}$, $d = 110\mu\text{m}$, and $\eta = 94\%$.

We further calculate the normalized phase responsivity (NR) to acoustic pressure and the relative contribution of S_L and S_n for a HC-PBF with the same outer diameter (including jacket), core size and air-filling ratio of 70 - 94% but with the thickness of the outer silica cladding ($c-b$) increased from 1 to 30 μm . The results are shown in Fig. 8(1) and 8(2) respectively. The results show that the NR of HC-PBF to acoustic pressure can be improved by optimizing the thickness of the fiber's silica cladding and the air-filling ratio; however the relative contribution of the refractive index, as compared to physical change of the fiber length, S_n/S_L remains being around -15%. Figure 9 shows the NRs as functions of the outer silica cladding thickness ($c-b$) with/without considering the effective index contribution (S_n), when the air-filling ratio is fixed at 94%. The calculated NR with S_n considered is $\sim 1.1 - 1.8$ dB lower than without considering S_n when the thickness of the outer silica-cladding ($c-b$) is varied from 1 to 30 μm .

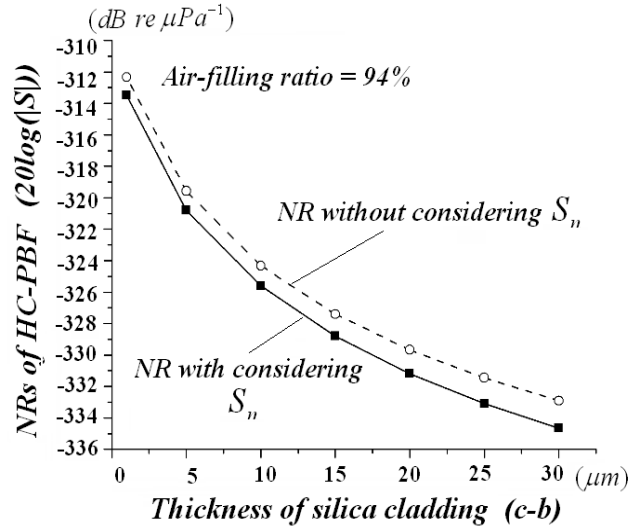


Fig. 9. NR of HC-PBF to acoustic pressure with/without considering S_n .

It is known that the mechanical properties (E_3 , ν_3) of the HC-PBF's polymer jacket material is uncertain because of the polymer material's flexible ingredient and fabrication process, and those properties may change with the environment. However, as mentioned in

Ref. 4, the dominant factor that determined the fiber's acoustic response is the thickness of its solid silica cladding, because the silica material has much higher Young's modulus than the outer polymer jacket. When the thickness of the outer polymer jacket is thin (e.g., tens of micrometers), the variation of mechanical properties of the fiber's outer jacket was found to have little effect on the HC-PCF's acoustic response. For example, when E_3 is varied from 0.5 to 1 MPa and ν_3 from 0.35 to 0.37, calculation shows that the NR of HC-1550-02 is changed by only ~0.4 dB.

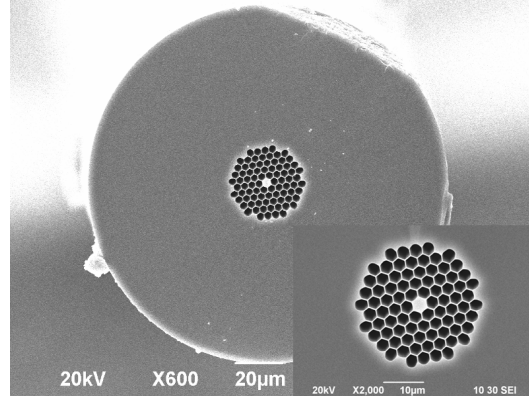


Fig. 10. SEM photograph of photonic crystal fiber (NL-3.3).

Our theoretical model was further applied to calculate the phase sensitivity of a non-linear photonic crystal fiber NL-3.3 [14] to axial strain. This fiber has a solid core and an air-silica cladding with air-filling ratio of ~84%. The air-silica cladding can also be approximately considered as uniform honeycomb structure. The SEM photograph of NL-3.3 is shown in Fig. 10 and its physical parameters are listed in Table 2.

At 1550nm, the effective refractive index of the fundamental mode of NL-3.3 fiber was calculated to be 1.4087, and the sensitivity of the mode-index to strain (dn_{eff}/ϵ) is $\sim -0.314 \epsilon^{-1}$. By using Eq. (3), the strain-sensitivity (S , S_L and S_n) are calculated to be $0.7773 \epsilon^{-1}$, $1 \epsilon^{-1}$ and $-0.2227 \epsilon^{-1}$, respectively. This is in good agreement with experimental result as will be presented in section 3.

Table 2. Physical parameters of NL-3.3

| Fiber | Pitch | η | a | b | c | d |
|--------|---------------------|----------|-----------------------|---------------------|---------------------|----------------------|
| | 3 (μm) | 84% | 1.65(μm) | 15(μm) | 75(μm) | 125(μm) |
| NL-3.3 | $E_0 = E_2$ | E_3 | $\nu_1 = \nu_2$ | ν_3 | n_0 | |
| | 72(GPa) | 0.5(GPa) | 0.17 | 0.37 | 1.444 | |

3. Experiment and results

The phase sensitivities of commercial HC-1550-02 and NL-3.3 fibers, with their cross-sections shown respectively in Fig. 11 and Fig. 10, to axial strain were experimentally measured. The experimental setup is shown in Fig. 12. A fiber-optic Michelson interferometer comprising of a 3-dB single mode fiber coupler, a sensing and a reference arm, is employed. Faraday rotation mirrors (FRMs) are used at the distal ends of both arms to avoid polarization induced signal fading. The interferometer was illuminated by an external cavity laser with a center wavelength of 1550nm and a line width of ~100 kHz. The HC-1550-02/NL-3.3 fiber was incorporated into the sensing arm of the interferometer, with one end spliced to one port of the 3-dB coupler and the other end to the pigtail of the FRM; the reference arm of the interferometer consisted of a similar length of SMF28 fiber splice to the second FRM.

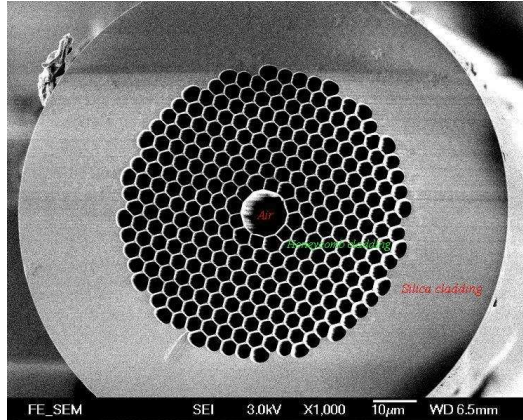


Fig. 11. SEM photograph of HC-PBF (HC-1550-02).

A standard strain test-rail was used to provide the axial strain to the sensing fiber. The sensing HC-PBF was fixed on the test-rail. The length of the sensing fiber is L . To measure phase sensitivity (S), one end of the rail was fixed, while the other end was computer controlled to move a known distance (ΔL). The output power variation of the interferometer and the moving distance of the test-rail were simultaneously recorded by the computer. The axial strain acting on the sensing fiber can be calculated by using $\varepsilon = \Delta L/L$. The phase sensitivity was then calculated from the measured number of fringes (N_f) for a given ΔL .

$$S = \frac{1}{\varphi} \frac{\Delta\varphi}{\varepsilon} = \left(\frac{1}{2}\right) \frac{\lambda N_f}{n_{\text{eff}} \Delta L}, \quad (20)$$

where the term $(1/2)$ in Eq. (20) is because the measurement was taken with a Michelson interferometer, in which the light goes through the sensing fiber twice. The experimental results agree well with the predicted values as summarized in Table 3. For sensitivity measurements of HC-1550-02 and NL-3.3 fibers, 258 and 129 fringes were respectively recorded with experimental inaccuracy of smaller than ± 1 fringes, corresponding to inaccuracy in S of $\sim \pm 0.004$ for HC-1550-02 and $\sim \pm 0.006$ for NL-3.3.

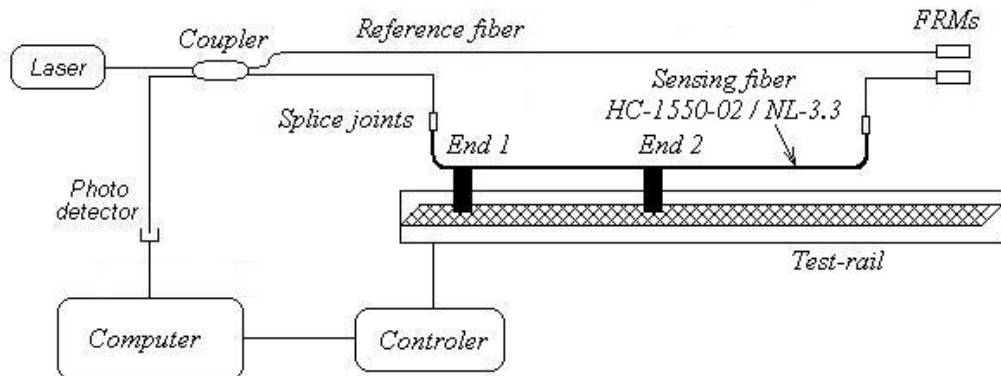


Fig. 12. Experimental setup.

Table 3. Measured S and predicted S, S_L, S_N of HC-1550-02/NL-3.3 to axial strain

| Fiber | Parameters | |
|------------|-----------------|---|
| HC-1550-02 | Predicted S_L | $1 \text{ } \varepsilon^{-1}$ |
| | Predicted S_n | $-0.0203 \text{ } \varepsilon^{-1}$ |
| | Predicted S | $0.9797 \text{ } \varepsilon^{-1}$ |
| | Measured S | $0.9815(\pm 0.004) \text{ } \varepsilon^{-1}$ |
| NL-3.3 | Predicted S_L | $1 \text{ } \varepsilon^{-1}$ |
| | Predicted S_n | $-0.2227 \text{ } \varepsilon^{-1}$ |
| | Predicted S | $0.7773 \text{ } \varepsilon^{-1}$ |
| | Measured S | $0.7813(\pm 0.006) \text{ } \varepsilon^{-1}$ |

For the measurement of phase sensitivity to acoustic pressure, the experimental setup and results have already been reported in the Ref. [4]. The experimentally measured and the theoretical results are summarized in Table 4. The experimentally measured $NR = -334.4 \text{ dB re } 1\mu\text{Pa}^{-1}$ is in good agreement with the theoretically result of $-333.1\text{dB re } 1\mu\text{Pa}^{-1}$. The prediction from the model with effective index contribution is closer to the experimental value than the result without considering the index term ($-331.6\text{dB re } 1\mu\text{Pa}^{-1}$) [4].

Table 4. Measured S and predicted S, S_L, S_N , and NR of HC-1550-02 PBF to acoustic pressure

| HC-1550-02 | Parameters | |
|--------------------------|------------------|--|
| Model Without Index-term | S | $-2.68*10^{-11}\text{Pa}^{-1}$ |
| | $NR = 20\log(S)$ | $-331.6 \text{ dB re } 1\mu\text{Pa}^{-1}$ |
| Model With Index-term | S_n | $4.64*10^{-12}\text{Pa}^{-1}$ |
| | S_L | $-2.68*10^{-11}\text{Pa}^{-1}$ |
| | S | $-2.216*10^{-11}\text{Pa}^{-1}$ |
| | $NR = 20\log(S)$ | $-333.1 \text{ dB re } 1\mu\text{Pa}^{-1}$ |
| Experiment | Measured NR | $-334.4 \text{ dB re } 1\mu\text{Pa}^{-1}$ |

4. Conclusion

In conclusion, we have investigated theoretically and experimentally the influence of strain and pressure to the effective refractive index of the fundamental-mode in HC-PBF. Theoretical modeling shows that the strain and pressure applied to the HC-PBF will cause the deformation of the HC-PBF's microstructure cladding and change the material index, and thus change of the effective index of the fiber's fundamental-mode. The modeling results for pressure is applicable to both hydrostatic and acoustic pressures. Using this theoretical model, an index-term of about $-2\%/ -17\%$ was predicted respectively for the phase sensitivity of the commercial HC-1550-02 PBF to the axial strain/acoustic pressure. The experimentally measured normalized phase sensitivities of the HC-1550-02 fiber to axial strain and acoustic pressure are respectively $0.9815 \text{ } \varepsilon^{-1}$ and $-2.216*10^{-11}\text{Pa}^{-1}$ ($-334.4\text{dB re } 1\mu\text{Pa}^{-1}$). These values agree well with our theoretical predictions. The theoretical model is also applicable to other hollow-core or solid-core photonic crystal fibers with high air-filling ratios.

Acknowledgement

The authors would like to acknowledge the support of the Hong Kong Special Administrative Region Government through a GRF grant PolyU5196/09E.